Parameters optimization of a walnut shell-kernel separation device using response surface methodology and ANN coupled genetic algorithm

Hualong Liu[1,2,3], Biqi Mao[1,2,3], Hong Zhang[1,2,3], Peiyu Chen[1,2,3], Yurong Tang[1,2,3], Xiuwen Fan[1,2,3], Yongcheng Zhang[1,2,3], Jianping Wang[1,2,3], Yong Zeng[1,2,3*]

(1. *College of Mechanical and Electronic Engineering, Tarim University, Alar, Xinjiang 843300, China*;
2. *Key Laboratory of Modern Agricultural Engineering, Tarim University, Alar, Xinjiang 843300, China*;
3. *Key Laboratory of Tarim Oasis Agriculture, Ministry of Education, Alar, Xinjiang 843300, China*)

Abstract: Walnut shell-kernel separation after cracking is crucial for providing raw materials for further processing. However, impurities and losses during separation limit complete separation. To address this, a two-stage tandem separation device was designed and optimized. Computational fluid dynamics (CFD) was used to analyze the effects of four bent duct structures on the flow field. Response surface methodology (RSM) and artificial neural networks (ANN) were employed to predict separation performance under various conditions. Both models accurately predicted performance, with ANN showing superior predictive ability. The optimal design was determined using non-dominated sorting genetic algorithm-II (NSGA-II) and technique for order preference by similarity to an ideal solution (TOPSIS): the inclination of the first stage deflector plate (x_1) was 39°,the inclination of the second stage deflector plate (x_2) was 36°, the wind speed of the first stage fan (x_3) was 21 m/s, and the wind speed of the second stage fan (x_4) was 13.5 m/s; impurity rate (y_1) was 4.51%, and loss rate (y_2) was 6.62%. Compared with traditional single-stage devices, the optimized device reduced impurity rate by 73.98% to 77.55% and loss rate by 9.44% to 53.96%, significantly improving separation efficiency and quality. This study provides theoretical guidance for designing and optimizing shell-kernel separation devices.

Keywords: walnut, two-stage separation device, multi-objective optimization, response surface methodology, artificial neural network

DOI: 10.25165/j.ijabe.20251805.9375

Citation: Liu H L, Mao B Q, Zhang H, Chen P Y, Tang Y R, Fan X W, et al. Parameters optimization of a walnut shell-kernel separation device using response surface methodology and ANN coupled genetic algorithm. Int J Agric & Biol Eng, 2025; 18(5): 306–316.

1 Introduction

Walnut (*Juglans regia* L.) is a famous dried fruit with an internal kernel and external shell. The kernel has high edible and medical value and can be made into snacks, drinks, oil, and other products[1,2]. However, in China, only about 20% of walnuts are processed due to outdated primary processing technologies (like drying and shelling) and high labor costs[3]. Separating the shell from the kernel is crucial but often leads to losses of up to 12% during processing[4]. This harms product quality and causes economic waste. Therefore, improving separation methods and developing better equipment are important for both food safety and economic efficiency.

In the past, various separation methods have been proposed according to different physical properties of shell and kernel. For example, an intelligent visual identification technique[5,6] is normally based on the varied color, texture, and morphological properties of shell and kernel, which can achieve accurate target classification. However, the properties of walnut shells and kernels have certain similarities, which brings great difficulty to separation. Meanwhile, this technique is not efficient. Electrostatic[7] and magnetic[8] separation methods are not only time-consuming and inefficient, but also have the potential to contaminate the kernel. Besides, the mixture of shell and kernel must be fully dried prior to the separation process to avoid significantly reducing the separation efficiency for the electrostatic method[4], which results in increasing unnecessary energy consumption. In summary, these separation methods are complex and have obvious drawbacks, which largely limit practical application. In recent years, the pneumatic separation that is cost-effective, simple, and easy to maintain, has been widely used in the separation of shell and kernel, especially for the agricultural materials including rice, rapeseed, and nut. Unfortunately, unexpected phenomena frequently occur during the separation process (e.g., containing impurities and entrainment loss), which limits the development and popularization of the pneumatic separation device. It is well known that the separation performance is strongly related to the physical characteristics of the shell and kernel (e.g., particle size and moisture content), configurations of separation devices (e.g., guide plate and length),

Received date: 2024-09-17 **Accepted date:** 2025-07-25

Biographies: Hualong Liu, PhD candidate, research interest: agricultural machinery, Email: HualongLiu6@126.com; **Biqi Mao**, PhD, Associate Professor, research interest: agricultural machinery, Email: maobiqi@126.com; **Hong Zhang**, Professor, research interest: agricultural machinery, Email: zhghog@163.com; **Peiyu Chen**, PhD, Associate Professor, research interest: agricultural machinery, Email: 1083830470@qq.com; **Yurong Tang**, MS, Senior Experimentalist, research interest: agricultural products processing technology, Email: 157723895@qq.com; **Xiuwen Fan**, MS, Associate Professor, research interest: agricultural machinery, Email: fanwenwen-1@163.com; **Yongcheng Zhang**, Master, Associate Professor, research interest: agricultural machinery, Email: yczh0802@163.com; **Jianping Wang**, Master, Associate Professor, research interest: agricultural machinery, Email: 5928853@qq.com.

***Corresponding author: Yong Zeng**, PhD, Associate Professor, research interest: agricultural machinery. College of Mechanical and Electronic Engineering, Tarim University, Alar 843300, Xinjiang, China. Tel: +86-15504577650; Email: yzengtarim@163.com.

and operational conditions (e.g., wind speed and deflector plate angle). Hence, many researchers have proposed a series of effective methods to improve separation performance in terms of the three aspects mentioned above, particularly the latter two factors.

Previous research has explored various aspects of separation devices. Li et al.[9] used ANN and RSM to study the effects of baffle opening and inlet angle on cleaning and loss rates in walnut shell-kernel winnowing devices. Zhang[10] optimized a separation device by considering walnut properties and apparatus structure. Drying walnuts for 30 min minimized suspension velocity overlap and maximized separation efficiency. CFD simulations further enhanced the device, achieving a cleaning efficiency of 91.86% and a loss rate of 4.42%. Safikhani[11] developed and optimized a Karagoz cyclone separator using NSGA-Ⅱ. Lim et al.[12] investigated how wind speed and water content affect separation performance in a jatropha fruit separator, noting that vortex flow increases particle residence time. Chen et al.[13] studied the relationship between airflow and loss in brown rice separation. However, single-pipeline separation devices struggle with multi-size and multi-component mixtures[14]. Wang et al.[15] proposed that adding a second separation stage improves density segregation, similar to cascade impactors used in agricultural material separation[16]. Examples include tandem two-stage separators for rice[17] and a two-stage winnower cyclone system[18]. Zhang and Liu[19] developed a two-stage tandem walnut shell-kernel separator and optimized its operational parameters using response surface methodology. The optimal parameter combination was identified, achieving a foreign material content of 4.75% and a kernel loss rate of 8.41%. Despite these advances, research on two-stage separation devices is limited due to their complexity in design and operation, requiring consideration of factors like airflow distribution and unit matching.

However, there is still a wide gap of knowledge about two-stage walnut shell-kernel separation that must be filled to truly understand the mechanism by which operating parameters affect device performance. Meanwhile, it is difficult to regulate the device and optimize its performance due to structural complexity. There is a need to better understand how operating parameters affect the performance of two-stage walnut shell-kernel separation devices. Therefore, designing a new two-stage separation device and optimizing its parameters is important. To achieve this, CFD simulations were used to study the flow inside the separation duct. RSM, ANN, and genetic algorithms were also applied to optimize the device's operating parameters (such as fan speeds and deflector plate angles). This approach helped create models to predict impurity and loss rates. Combining RSM, ANN, and NSGA-Ⅱ proved to be effective for optimizing the device's performance.

2 Materials and methods

2.1 Materials

'Wen 185' was chosen as the experimental specimen in this study, which is the typical walnut cultivar in the local market. Fresh-harvested walnuts were collected on September 15, 2022, from the Wensu Walnut Experimental Station (latitude: 41°27′67″N, longitude: 80°24′17″E, and altitude: 1056 m), Xinjiang, China. Walnuts were cracked using a multi-point extrusion cracking device under optimum operating parameters (cracking angle 0.47° and roller speed 108 r/min), which shows a cracking rate of 97.24% and a high-quality kernel rate of 92.3%[20]. Moreover, secondary cracking was implemented to crack unbroken walnuts. After that, the dry base moisture contents of shell and kernel as well as diaphragma juglandis fructus were measured using the standard hot air oven method, and the values (average of three experiments) were 8.46%, 12.01%, and 28.32%, respectively. As shown in Figure 1, walnut shell and kernel were manually classified into 1/8, 1/4, and 1/2 grades according to their size. Notice that 1/2 kernel and 1/4 kernel are defined as high-quality kernels in this study.

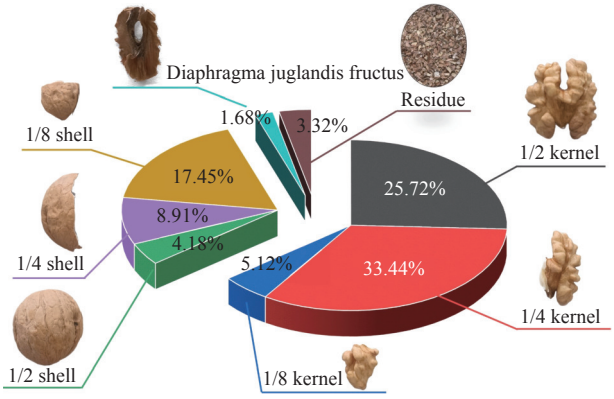

Figure 1 Proportions of the components of the mixture

2.2 Development of walnut shell-kernel separation device

A two-stage tandem walnut shell-kernel separation device, as shown in Figure 2a, including the frame, feed device, frequency control box, first stage separation duct, second stage separation duct, and cyclone separator, was designed and manufactured. The discharging outlet of the first stage separation device is connected with the feeding inlet of the second stage separation device, and each comes complete with a centrifugal fan (DF-2.5-Ⅱ and Ⅲ, China). Each separation duct consists of an air inlet, a feeding inlet, a collecting outlet, a discharging outlet, and a deflector plate. To meet the requirements of different working conditions, a frequency control box was used to adjust wind speed and the speed of the feed roller. The function of the deflector plate was to prevent the materials from undergoing centrifugal motion along the inner wall of the bent duct and to make their motion more dispersed.

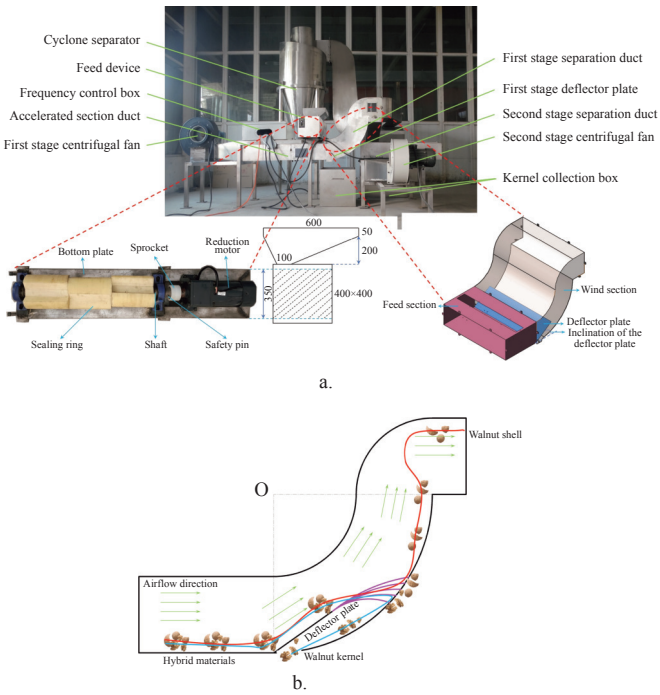

Figure 2 Schematic diagram of walnut shell-kernel separation device and the deflector plate mechanism

The separation process uses a deflector plate and centrifugal

action to sort particles by size (Figure 2b). The deflector plate is essential, as it redirects airflow to counteract centrifugal forces, ensuring uniform pressure distribution and enhancing system stability and efficiency. Without it, airflow would be uncontrolled, leading to increased centrifugal effects, uneven distribution, component wear, and reduced performance. The angled deflector plate prevents walnut shells and kernels from clustering along the duct wall, improving particle distribution and separation efficiency. At optimal wind speeds, kernels fall into a collection box due to gravity, while lighter shells are carried away. The two-stage design captures high-quality kernels in the first stage and separates crushed kernels in the second, with residue and dust directed to a cyclone separator. This yields three outputs: high-quality kernels, crushed kernels, and walnut shells. The process can be adjusted for different mixtures by modifying wind speed and deflector plate angles. Detailed device dimensions are listed in Table 1.

Table 1 Parameters of the separation equipment

Parameters	Size
Material	GB-0Cr18Ni9 (China)
Overall size, length × width × height/mm	2600 × 2600 × 2600
Hopper, length × height/mm	400 × 200
Separation duct, width × thickness/mm	600 × 226
Bend radius/mm	550
Cyclone separator inside diameter/mm	560
Overall weight/kg	350
Maximum capacity/kg·h^{-1}	720
Inclination of the deflector plate/(°)	20-60
First stage centrifugal fan	DF-2.5-Ⅲ (China)
Second stage centrifugal fan	DF-2.5-Ⅱ (China)

2.3 Numerical simulation

2.3.1 Governing equation

The standard k-ε model in ANSYS Fluent 19.2 was used to simulate fluid flow in 90° bends. Validated in prior studies[21,22], it uses continuity and momentum equations. For detailed equations, refer to Dai et al.[22]

2.3.2 Simulation model and boundary conditions

A simplified three-dimensional model of the two-stage tandem shell-kernel separation device was created in SolidWorks 2018 to determine the bent duct radius (Figure 3a). Different colored lines indicate various duct curvatures. The simulation employed the SIMPLEC, PRESTO, and QUICK schemes for pressure-velocity coupling and spatial discretization due to their convergence advantages. A no-slip boundary condition and standard wall function were applied, with a velocity inlet of 20 m/s and a pressure outlet. The fluid was air (viscosity: 1.8×10^{-5} Pa·s, density: 1.2 kg/m^3), and the flow was assumed incompressible. The simulation used a convergence accuracy of 0.001, a time step of 0.01 s, and ran for 10 s.

2.3.3 Mesh division and mesh independence testing

Grid independence verification was conducted to balance computational accuracy and efficiency. For models with a bending outer radius of 550 mm, simulations with grids of 90 698, 105 846, 117 514, 122 225, and 140 205 cells were performed to assess the impact of grid quantity on pressure drop and tangential velocity. The grid count was adjusted by varying cell sizes, while maintaining a maximum skewness below 0.6 and mesh quality within a range of 0.3-1.0. As shown in Figure 4a, pressure drop was calculated using the method by Le and Yoon[23], and Figure 4b illustrates tangential velocity trends at the r = 350 mm cross-section.

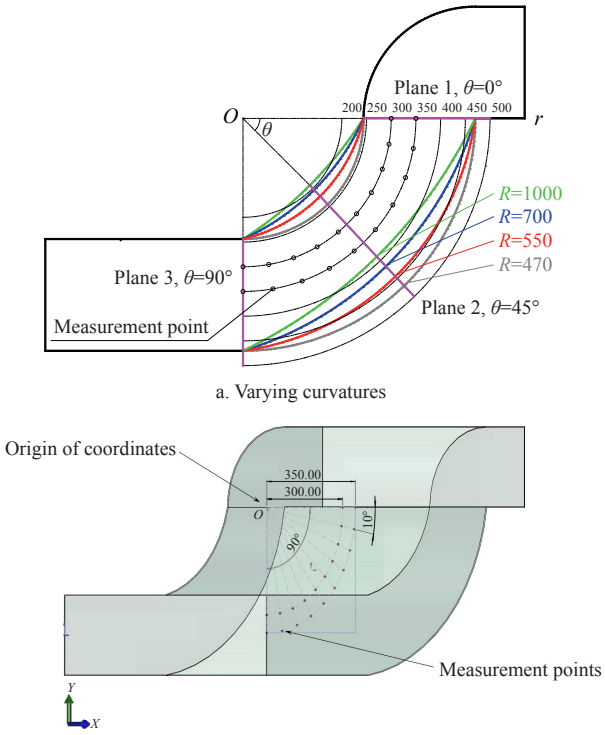

a. Varying curvatures

b. Measurement point

Figure 3 Three-dimensional model of separation ducts

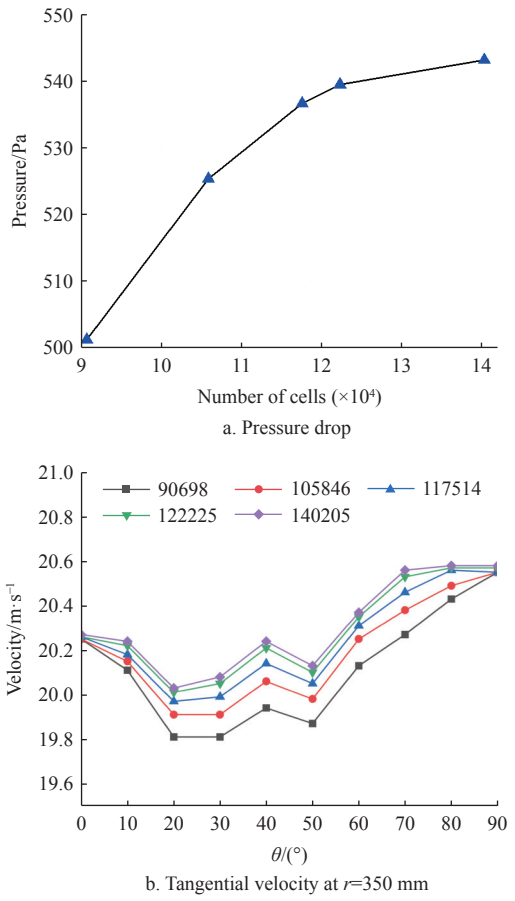

a. Pressure drop

b. Tangential velocity at r=350 mm

Figure 4 Grid independence verification

When the grid count reached 122 225 cells, pressure drop and tangential velocity stabilized with a relative error of less than 1%. Therefore, the grid domain for the 550 mm radius was set to 122 225 cells (Figure 5). Similarly, grid domains for radii of 470 mm, 700 mm, and 1000 mm were established with 125 305,

120 115, and 114 215 cells, respectively.

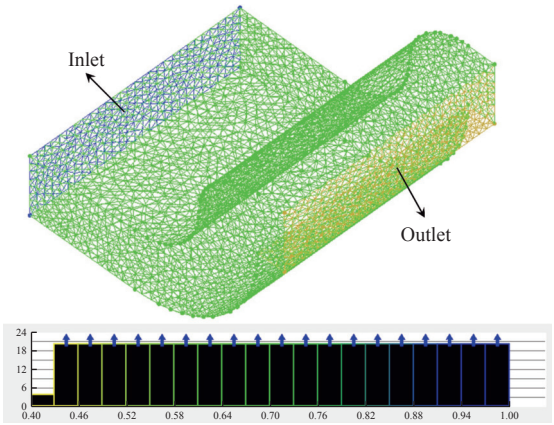

Figure 5 Mesh structure of bent duct

2.4 Predictive modeling and optimization methods

2.4.1 RSM modeling

Response surface method (RSM) is an empirical modeling system based on linear models that could be utilized for developing, improving, and optimizing complex processes[24]. It has the advantage of providing statistically acceptable findings with fewer tests[25]. RSM model fits complex unknown functional relationships in a small region with a simple primary or quadratic polynomial model, which is an effective means of solving parametric optimization problems. On the basis of preliminary tests and single factor tests, input parameters and their respective ranges of values were determined (i.e., $34 \le x_1 \le 42$, $30 \le x_2 \le 38$, $18 \le x_3 \le 22$, and $12 \le x_4 \le 16$). The central composite design (CCD) method was applied to develop the design space and obtain sampling points. Each design variable has five different levels (including three points within the limits specified for each factor and two points outside those limits)[26], including the inclination of the first stage deflector plate (x_1: 34°, 36°, 38°, 40°, 42°), the inclination of the second stage deflector plate (x_2: 30°, 32°, 34°, 36°, 38°), the wind speed of the first stage fan (x_3: 18, 19, 20, 21, 22 m/s),and the wind speed of the second stage fan (x_4: 12, 13, 14, 15, 16 m/s). The objective functions were impurity rate (y_1) and loss rate (y_2). The number of required tests (N) was defined as $N = n_0 + 2K + 2^K$, in which K and n_0 are the number of design variables and the number of central points, respectively[27].

2.4.2 ANN modeling

RSM is simple but cannot capture all features of complex nonlinear responses[28]. ANN, however, is more sophisticated and powerful for modeling nonlinear interactions between variables, making it popular for optimizing agricultural equipment parameters[9]. But ANN needs lots of data to avoid overfitting, so data collection takes longer than for RSM[28]. Fortunately, RSM data can be sufficient for effective ANN models if it has good statistical distribution[27]. In this study, ANN models for impurity rate and loss rate were built using limited RSM data (30 samples). K-fold cross-validation was used to make the most of the data by dividing it into subsets for training, validation, and testing. This method helps prevent overfitting and underfitting, providing reliable performance estimates. Here, five-fold cross-validation was applied, dividing the 30 samples into five groups of six. Each group was used once for testing, once for validation, and the remaining for training, repeated five times and averaged to assess model performance. The ANN model used a three-layer feed-forward backpropagation network with Levenberg-Marquardt training, tangent sigmoid activation for hidden layers, and linear activation for output. Design variables (x_1, x_2, x_3, x_4) were inputs, and objective functions (y_1, y_2) were outputs. The optimal number of neurons in the single hidden layer was determined by trial-and-error to minimize mean square error.

2.4.3 Optimization method

The significance of the optimization procedure is obtaining the optimal values of the operating parameters that minimize impurity rate and minimum loss rate. To obtain globally optimal results, NSGA-Ⅱ algorithm was used. NSGA-Ⅱ performs optimization using non-dominated sorting and elite policies with congestion distance optimizer operators. Compared with the weighting method, NSGA-Ⅱ has the advantage of uniform distribution of the Pareto solution set, which is suitable for multi-objective solution of non-convex problems. In addition, it avoids time-consuming problems, and all the optimal solutions can be obtained by solving Pareto only once. In this process, the adaptation function is the RSM or ANN prediction model, with a population size of 100 individuals, and 10 000 iterations, and a crossover and mutation percentage of 90% and 10%, respectively[29].

The NSGA-Ⅱ process consists of the following steps: First, it initializes the population and assesses the fitness of individuals. Then, a non-dominated sorting is performed to categorize the individuals into different classes, and the crowding degree of each individual is calculated. Next, new populations are generated using selection, crossover, and mutation operations. Finally, combining the parent and offspring populations, non-dominated sorting and crowding comparisons are performed to select the next generation of populations. The optimization process is wrapped up with the condition of repetitions.

When solving objective functions, constraints are needed to limit them. The design variable constraints restrict the range of values of each design variable. The value ranges are as follows:

$$\begin{cases} \text{Min}\{y_1(x_1,x_2,x_3,x_4)\} \\ \text{Min}\{y_2(x_1,x_2,x_3,x_4)\} \\ \text{s.t.} \begin{cases} 34^\circ \le x_1 \le 42^\circ \\ 30^\circ \le x_2 \le 38^\circ \\ 18\ \text{m/s} \le x_3 \le 22\ \text{m/s} \\ 12\ \text{m/s} \le x_4 \le 16\ \text{m/s} \end{cases} \end{cases} \tag{1}$$

where, y_1 is the impurity rate, %; y_2 is the loss rate, %; Min $\{y_1(x_1, x_2, x_3, x_4)\}$ is the objective function for minimizing the impurity rate; Min $\{y_2(x_1, x_2, x_3, x_4)\}$ is the objective function for minimizing the loss rate; x_1 is the inclination of the first stage deflector plate, (°); and x_2 is the inclination of the second stage deflector plate, (°); x_3 is the wind speed of the first stage fan, m/s; x_4 is the wind speed of the second stage fan, m/s.

2.5 Evaluation index

The objective functions, including impurity rate (y_1) and loss rate (y_2), were calculated using the methods of Zhang et al.[30] and Wang et al.[31]

$$y_1 = \frac{m_i}{m_t} \times 100\% \tag{2}$$

$$y_2 = \frac{m_k}{m_{kt}} \times 100\% \tag{3}$$

where, m_i is mass of impurities in collection box of kernels, kg; m_t is mass of kernels in collection box of kernels, kg; m_k is mass of kernels in collection box of shells, kg; m_{kt} is total mass of collection box of kernels, kg.

3 Results and analysis

3.1 Simulation analysis

3.1.1 Validation of numerical model

To verify the simulation results, they were compared with experimental data from a hot-wire anemometer. The probe had a 5 μm tungsten filament, with response and acquisition frequencies of 25 kHz and 100 kHz, respectively. The duct was cleaned with cotton cloth and alcohol to reduce dust. Tangential velocities were measured at different positions in the curved duct (r = 300 mm and r = 350 mm, Figure 3b). The simulation results were compared with the average of three experiments using the anemometer (AR866A, Smart Sensor). Following Yang et al.[32], the probe was positioned using stepper motors to measure the flow field at any point. Finite positioners ensured consistent measurement point distribution. Figure 6 shows the tangential velocities, with errors within 5%. The good agreement validates the model, despite disturbances from the probe and factors like turbulent diffusion and boundary conditions.

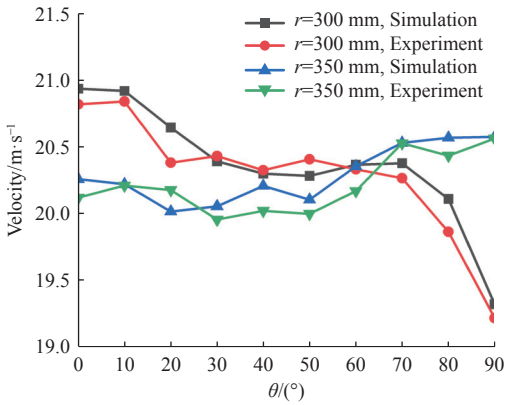

Figure 6 Tangential velocities at r = 300 and 350 mm in the bent duct

3.1.2 Distribution of the pressure field

To analyze the internal flow field in the separation device, a polar coordinate system (origin at point O) was established to observe the flow field distribution (Figure 3b). Here, θ is the polar angle, and r is the polar diameter. The side near O is the inside of the bent duct, while the side away from O is the outside. Three axial sections were taken at θ = 0°, 45°, and 90° to form planes 1, 2, and 3. The pressure drop is crucial for the separating device as it indicates energy loss[33]. Figure 7 shows the steady-state pressure distribution in circumferential and axial sections under various operating conditions. The small axial pressure gradient variation suggests that the duct design reduces its impact on the flow field, minimizing particle back-mixing[34]. Due to centrifugal force, flow accelerates near the outer region of the bent duct, while the inner region has lower pressure. As the radius increases, the pressure gradient decreases in planes 1 and 2, indicating higher pressure loss, while it increases in plane 3. Wall pressure on planes 1 and 2 decreases with increasing radius, as does the upper wall pressure on plane 3. This is because a smaller radius reduces centrifugal resistance, lowering the pressure gradient but increasing upper wall pressure[35].

The static pressure decreases when the air flow enters the separating device and passes through the bent duct, resulting in a large pressure gradient. This is mainly due to the rotational acceleration of the air flow in the separating device, which converts a portion of the static pressure into kinetic energy while overcoming the resistance. A more significant pressure difference exists between the inside and outside of the bent duct. Among them, the pressure reaches a maximum value when passing through the outer bend, whereas the pressure reaches a minimum value when the fluid flows through the inner bend, and a negative pressure is also generated on the inner side of the bend. A similar phenomenon was reported by Liu et al.[21] This is because fluid flow direction changes in the bending section due to the constraint of the outer wall surface. In the centrifugal force, fluid has a tendency to get out of the mainstream, which makes the inner side of the pressure smaller and the outer side of the pressure value larger[36]. The higher the degree of bending and the sharper the change in the direction of fluid movement, the greater the local resistance loss is. Similarly, Jiang et al.[37] conducted a numerical study on the flow and heat transfer characteristics of a 90° bend extruded pipe and came to the same conclusion. The radius of the bent duct is within the range of 550-700 mm, except that when r = 250 mm, the airflow pressure changes significantly, and the rest of the airflow pressure fluctuations are small and relatively stable.

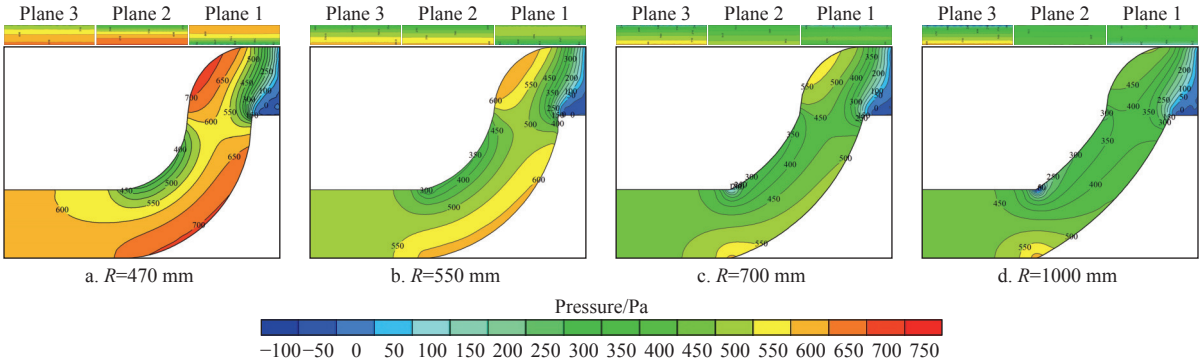

Figure 7 Distribution of the pressure at different cross-sections in the axial and circumferential directions

The analysis of the pressure flow field shows that as the radius of the bent duct increases, the pressure gradient decreases while the airflow pressure loss increases. This is mainly due to the abrupt change in flow direction at the bend, which causes localized losses. When the duct radius is 550 mm, the pressure gradient is below 100 Pa, and the pressure loss is minimal, indicating a more uniform distribution of the pressure flow field.

3.1.3 Distribution of the velocity of the flow field

To understand how the radius of the bent duct affects the flow field in the separation device, the steady-state velocity distribution at circumferential and axial positions was analyzed under various working conditions (Figure 8). The velocity near the wall approaches zero without generating local disturbances. The airflow velocity gradient increases in planes 1 and 2 as the duct radius

increases, but decreases in plane 3. This is because higher velocity is needed to overcome centrifugal force in plane 3. Du et al.[38] found that airflow velocity shows horizontal stratification, causing different materials to follow different trajectories. Plane 1 has the most uniform and stable flow field, indicating that the duct radius significantly affects airflow distribution.

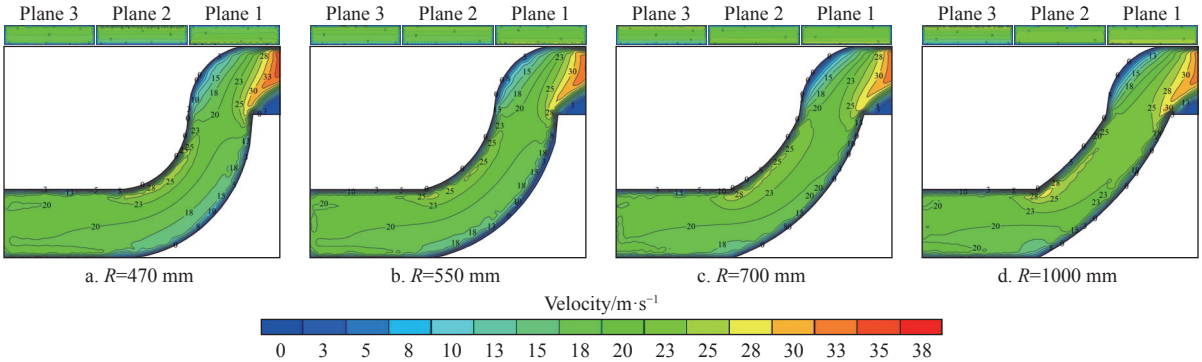

Figure 8 Distribution of the velocity of circumferential and axial sections under different working conditions

Figure 8 shows the velocity distribution in the circumferential section at different locations and conditions. As the radius of the bent duct increases, the airflow velocity decreases slightly, and the velocity gradient first decreases and then increases. The flow direction remains relatively stable overall. According to Liu et al.[21], the velocity distribution is opposite to the pressure distribution: velocity is lowest in the outer bent duct and highest in the inner bent duct. This is because the fluid is compressed by the lower pressure on the outer side, increasing its velocity. At the upper and lower centers of the bent duct (r = 300 mm and r = 350 mm), velocity fluctuations are smooth. The airflow velocity is relatively stable with some fluctuations when the radius is 470-550 mm. The velocity of the 250 mm curve changes violently at the 470 mm radius due to fluid viscosity, while the velocity of the 400 mm curve changes significantly at radii of 700-1000 mm.

The analysis results of the velocity flow field are as follows: with the increase in the radius of the bent duct, the velocity flow field becomes less stable, the velocity fluctuation in the wall area of the flow field changes more drastically, and the velocity loss gradually becomes larger, which increases the velocity of the airflow in the tube and thus makes the particles have greater rotational momentum. When the radius of the duct is 550 mm, the overall wind velocity gradient of the flow field is less than 2 m/s, and the velocity flow field is more uniform.

In summary, the pressure field and velocity field in the separation duct are evenly distributed when the duct radius is 550 mm, so the radius of the bent duct is designed to be 550 mm.

3.2 Analysis of RSM

The experimental scheme and the results (average of three experiments) are summarized in Table 2. The precision of the quadratic models is checked by analysis of variance, and the results are cataloged in Table 3. For the impurity rate model, the value of R^2 is 0.9716; the loss of fit (p = 0.1256 > 0.05) is not significant, while the model is extremely significant (p < 0.01), which indicates an impurity rate model could be used to analyze and predict the impurity content. For the loss rate model, the value of R^2 is 0.9711; the loss of fit (p = 0.1038 > 0.05) is not significant, while the model is extremely significant (p < 0.01), indicating the absence of other major design variables affecting the response value. The final equation in terms of coded factors:

$$\begin{aligned} y_1 =& 4.98 - 0.13x_1 + 0.081x_2 - 0.85x_3 - 0.52x_4 + 0.068x_1x_2 + \\ & 0.066x_1x_3 - 0.37x_1x_4 + 0.064x_2x_3 + 0.35x_2x_4 + 0.22x_3x_4 + \\ & 0.12x_1^2 + 0.28x_2^2 + 0.073x_3^2 + 0.21x_4^2 \end{aligned} \quad (4)$$

$$\begin{aligned} y_2 =& 8.24 - 0.52x_1 + 0.47x_2 + 0.9x_3 + 0.88x_4 + 0.18x_1x_2 + 0.042x_1x_3 + \\ & 0.65x_1x_4 - 0.3x_2x_3 - 0.068x_2x_4 - 0.39x_3x_4 + 0.27x_1^2 + 0.49x_2^2 + \\ & 0.05x_3^2 + 0.1x_4^2 \end{aligned} \quad (5)$$

Within the bounds of the analyzed design variables, the model generated above accurately predicted impurity rate and loss rate. For RSM regression model, the maximum relative errors of the training results for the impurity rate and loss rate models were 6.42% and 5.34%, respectively. Most of the residuals are close to zero, with the highest residual values of 0.26 and 0.58 for the impurity rate and loss rate models, respectively, and the lowest residual values of –0.38 and –0.37, respectively, indicating that the models constructed have high accuracy.

The effects of design variables x_1, x_2, x_3, and x_4 on response values y_1 and y_2 were analyzed and visualized in 3D diagrams (Figure 9). More curved lines in the 3D plots indicate greater influence of the design variables. Contour plots with elliptical shapes and large curvatures suggest significant interactions between variables. The color gradient from blue to red represents increasing extract mass, with faster color changes indicating steeper slopes and stronger impacts on the results.

3.3 Analysis of ANN

The optimal topologies for the impurity and loss rate models were determined by trial-and-error method to be 4-10-1. For the impurity rate, R^2 = 0.9883, MSE = 0.012 76, and RMSE = 0.1130; for the loss rate, R^2 = 0.9854, MSE = 0.033 77, and RMSE = 0.1838. For the ANN model, the maximum relative errors of the training results for the impurity and loss rate models were 4.64% and 3.79%, respectively. Most of the residuals are close to zero, with the highest residual values of 0.27 and 0.35 for the impurity rate and loss rate models, respectively, and the lowest residual values of –0.21 and –0.39, respectively, indicating that the models constructed have high accuracy.

3.4 Comparison of RSM and ANN

The fitness of ANN and RSM models was investigated through the values of R^2, MSE, and RMSE[39]. Among these, the higher the value of R^2, the closer it is to 1, indicating a greater degree of correlation between the measured and predicted values. The larger values of MSE and RMSE imply a higher likelihood of error in prediction. The results show that R^2 of the RSM model for the impurity rate (0.9716) is significantly lower than that of the ANN model (0.9883). The RSM model also has a higher MSE (0.026 60) and RMSE (0.1631) than the ANN model (MSE = 0.012 76, RMSE = 0.1130). The R^2 of the RSM model for the loss rate

Table 2 RSM measured and predicted responses

Test No.	x_1/(°)	x_2/(°)	x_3/m·s^{-1}	x_4/m·s^{-1}	y_1/%			y_2/%		
					Experimental	RSM	ANN	Experimental	RSM	ANN
1	36 (–1)	32 (–1)	19 (–1)	13 (–1)	7.40	7.49	7.48	7.39	7.55	7.45
2	40 (1)	32 (–1)	19 (–1)	13 (–1)	7.61	7.70	7.54	4.69	4.78	4.68
3	36 (–1)	36 (1)	19 (–1)	13 (–1)	6.91	6.70	6.74	9.14	8.89	9.36
4	40 (1)	36 (1)	19 (–1)	13 (–1)	7.40	7.18	7.51	6.40	6.74	6.16
5	36 (–1)	32 (–1)	21 (1)	13 (–1)	4.96	5.08	4.91	10.32	10.54	10.29
6	40 (1)	32 (–1)	21 (1)	13 (–1)	5.75	5.55	5.68	7.88	8.03	7.96
7	36 (–1)	36 (1)	21 (1)	13 (–1)	4.77	4.55	4.87	10.51	10.76	10.48
8	40 (1)	36 (1)	21 (1)	13 (–1)	5.08	5.29	5.19	9.24	8.86	8.89
9	36 (–1)	32 (–1)	19 (–1)	17 (1)	6.18	6.05	6.23	8.55	8.92	8.85
10	40 (1)	32 (–1)	19 (–1)	17 (1)	4.72	4.78	4.69	8.95	8.68	8.96
11	36 (–1)	36 (1)	19 (–1)	17 (1)	6.62	6.65	6.61	10.08	9.91	10.03
12	40 (1)	36 (1)	19 (–1)	17 (1)	5.70	5.66	5.72	10.86	10.28	11.25
13	36 (–1)	32 (–1)	21 (1)	17 (1)	4.47	4.52	4.53	10.82	10.45	10.53
14	40 (1)	32 (–1)	21 (1)	17 (1)	3.23	3.52	3.38	10.23	10.46	10.25
15	36 (–1)	36 (1)	21 (1)	17 (1)	5.40	5.39	5.40	10.41	10.31	10.34
16	40 (1)	36 (1)	21 (1)	17 (1)	4.91	4.65	5.12	11.12	10.94	11.06
17	34 (–2)	34 (0)	20 (0)	14 (0)	5.64	5.74	5.71	10.44	10.37	10.38
18	42 (2)	34 (0)	20 (0)	14 (0)	5.21	5.21	5.21	8.12	8.23	8.18
19	38 (0)	30 (–2)	20 (0)	14 (0)	6.18	5.95	6.01	9.58	9.27	9.36
20	38 (0)	38 (2)	20 (0)	14 (0)	5.92	6.30	5.65	10.75	11.09	10.97
21	38 (0)	34 (0)	18 (–2)	14 (0)	6.85	6.97	6.95	6.63	6.59	6.64
22	38 (0)	34 (0)	22 (2)	14 (0)	3.59	3.56	3.58	10.17	10.24	10.19
23	38 (0)	34 (0)	20 (0)	12 (–2)	6.73	6.86	6.81	7.20	6.89	7.15
24	38 (0)	34 (0)	20 (0)	16 (2)	4.82	4.78	4.86	10.00	10.34	9.68
25	38 (0)	34 (0)	20 (0)	14 (0)	5.05	4.94	4.98	7.96	8.14	8.23
26	38 (0)	34 (0)	20 (0)	14 (0)	4.76	4.94	4.95	8.34	8.14	8.23
27	38 (0)	34 (0)	20 (0)	14 (0)	4.81	4.94	4.95	8.48	8.14	8.23
28	38 (0)	34 (0)	20 (0)	14 (0)	5.07	4.94	4.95	7.94	8.14	8.23
29	38 (0)	34 (0)	20 (0)	14 (0)	5.07	4.94	4.95	8.37	8.14	8.23
30	38 (0)	34 (0)	20 (0)	14 (0)	5.11	4.94	4.95	8.32	8.14	8.23

Table 3 Analysis of variance applying RSM model

Origin	Impurity rate (y_1)					Loss rate (y_2)				
	Squares	df	Mean square	F-value	p-value	Squares	df	Mean square	F-value	p-value
Model	32.78	14	2.34	44.79	< 0.0001 **	68.69	14	4.91	38.07	< 0.0001 **
x_1	0.42	1	0.42	8.01	0.0127 *	6.50	1	6.50	50.44	< 0.0001 **
x_2	0.16	1	0.16	3.03	0.1022	5.29	1	5.29	41.06	< 0.0001 **
x_3	17.49	1	17.49	334.58	< 0.0001 **	19.35	1	19.35	150.14	< 0.0001 **
x_4	6.48	1	6.48	123.92	< 0.0001 **	18.46	1	18.46	143.26	< 0.0001 **
x_1x_2	0.074	1	0.074	1.42	0.2519	0.49	1	0.49	3.83	0.0692
x_1x_3	0.069	1	0.069	1.32	0.2689	0.028	1	0.028	0.22	0.6475
x_1x_4	2.18	1	2.18	41.75	< 0.0001 **	6.83	1	6.83	52.96	< 0.0001 **
x_2x_3	0.066	1	0.066	1.27	0.2778	1.48	1	1.48	11.50	0.0040 **
x_2x_4	1.95	1	1.95	37.35	< 0.0001 **	0.074	1	0.074	0.58	0.4596
x_3x_4	0.79	1	0.79	15.06	0.0015 **	2.39	1	2.39	18.58	0.0006 **
$(x_1)^2$	0.43	1	0.43	8.13	0.0121 *	1.99	1	1.99	15.48	0.0013 **
$(x_2)^2$	2.16	1	2.16	41.34	< 0.0001 **	6.61	1	6.61	51.30	< 0.0001 **
$(x_3)^2$	0.15	1	0.15	2.81	0.1142	0.068	1	0.068	0.53	0.4797
$(x_4)^2$	1.23	1	1.23	23.57	0.0002 **	0.27	1	0.27	2.11	0.1665
Residual	0.78	15	0.052			1.93	15	0.13		
Lack of fit	0.67	10	0.067	2.90	0.1256	1.67	10	0.17	3.23	0.1038
Pure error	0.12	5	0.023			0.26	5	0.052		
Cor total	33.57	29				70.62	29			
R^2			0.9716					0.9711		
MSE			0.026 60					0.068 57		
RMSE			0.1631					0.2619		

Note: "**" means extremely significant ($p < 0.01$); "*" means significant ($p < 0.05$).

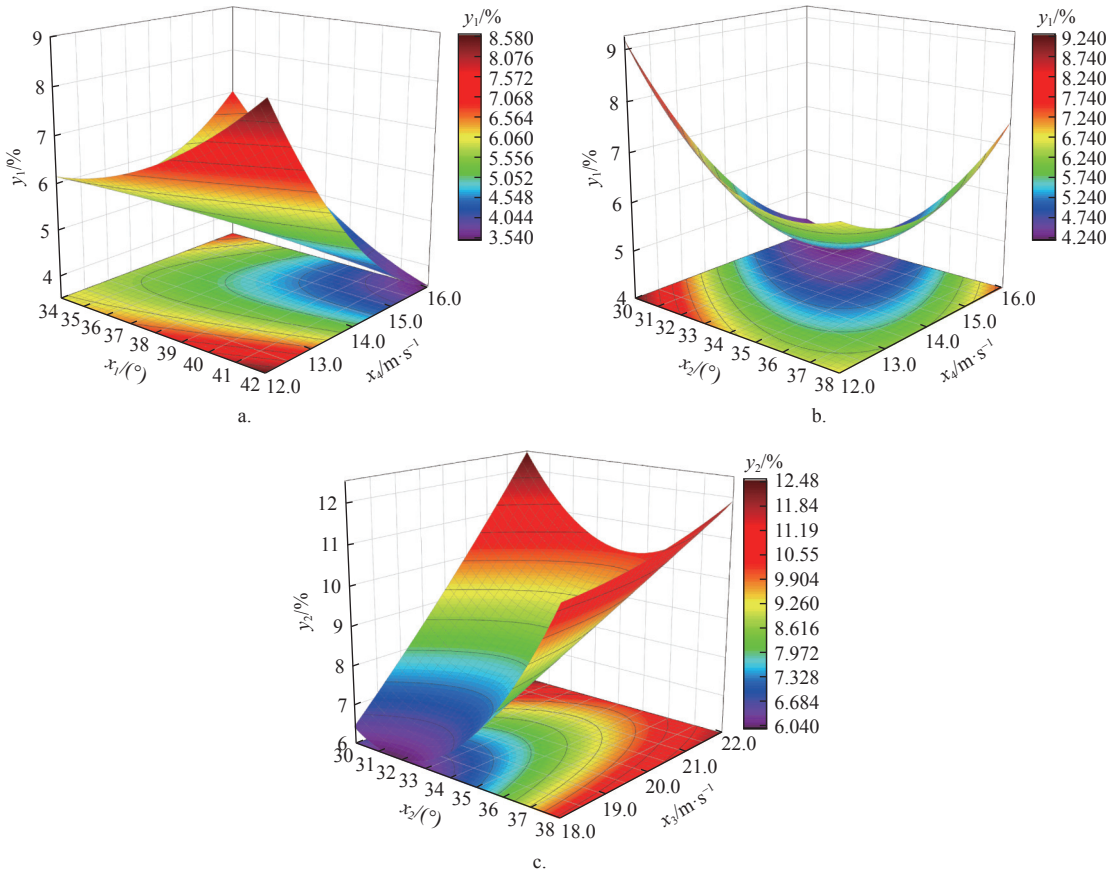

Figure 9 Interaction of operating parameters on impurity rate (y_1) and loss rate (y_2)

(0.9711) is significantly lower than that of the ANN (0.9854). The RSM model also has a higher MSE (0.068 57) and RMSE (0.2619) than the ANN model (MSE = 0.033 77, RMSE = 0.1838). The above analysis suggests a higher R^2 value of the ANN model compared with the RSM model, which demonstrates the superiority of the ANN model in terms of predictive and estimation capabilities. The lower MSE and RMSE values indicate that the ANN model possesses better prediction and generalization characteristics to the experimental data. The ANN model has a high prediction accuracy, which is attributed to its broad adaptability to the nonlinear behavior of the system, while the RSM model is limited by second-order polynomial regression.

The fitness of ANN and RSM models are further evaluated by comparing predicted and experimental values (Figure 10). It can be seen that the experimental and predicted data of each experimental run have high consistency and correlation. The ANN model has higher accuracy than the RSM model because the curve of the ANN is closer to the experimental data than the RSM. In summary, the ANN model has higher prediction accuracy than the RSM model. As it turns out, the data collected by RSM is sufficient for constructing effective ANN models when the data has a good statistical distribution in the input domain.

3.5 Multi-objective optimization

3.5.1 Analysis of optimization solutions

In multi-objective optimization, the optimal solution for each generation is obtained using NSGA-Ⅱ optimization and compared with the previous generations. Pareto optimal fronts (a vector set composed of objective function values) are shown in Figure 11. Note that in Pareto optimal solution sets with 100 individuals, all points obtained are optimal, which means the points are not superior to each other. In other words, if one objective function becomes better, the other objective function will inevitably become worse[31].

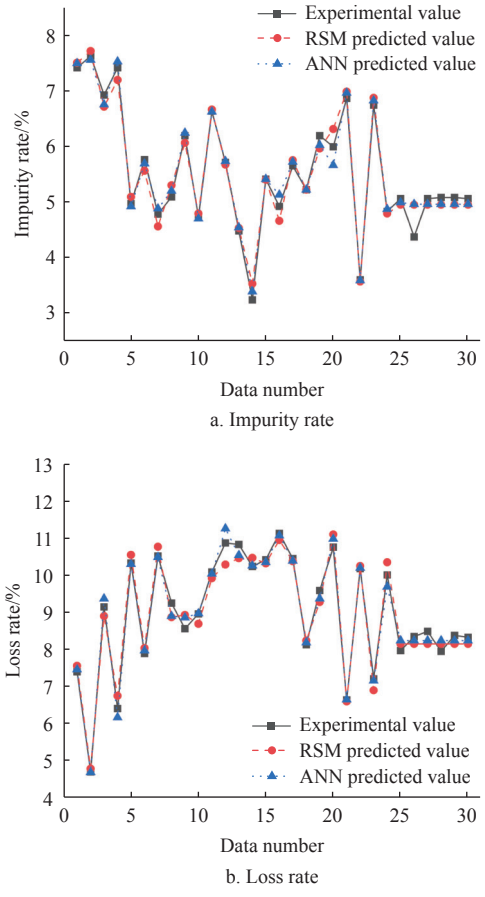

Figure 10 Comparison of predictions with experimental values

To aid the designer in selecting the appropriate operating parameter of a walnut shell-kernel separation device for different situations,

the correlation between the impurity rate (y_1) and loss rate (y_2) is fitted in the form of an empirical function as follows:

$$y_2 = 26.03 \times e^{-\frac{y_1}{2.29}} + 2.95 \quad (6)$$

As seen from the above plots, all objective functions change continually with the various design variables. To balance the economy and quality of the production and processing, after determining the positive ideal solution and the negative ideal solution of all individuals by technique for order preference by similarity to an ideal solution (TOPSIS). The optimal solution is quantitatively selected with x_1 at 38.78°, x_2 at 36.10°, x_3 at 20.93 m/s, and x_4 at 13.50 m/s, at which time impurity rate is 4.37% and loss rate is 6.39%.

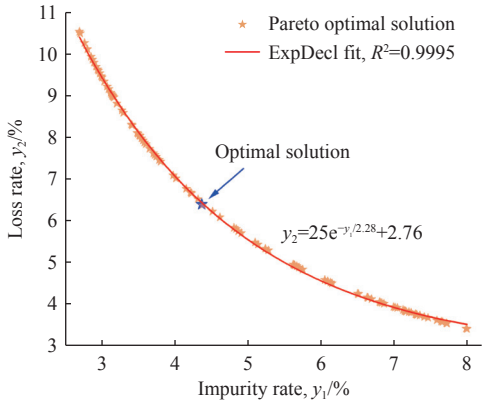

Figure 11 Distribution of Pareto optimal solution sets

3.5.2 Verification of optimal solution

The ANN model deviated from the actual result to a certain extent, which may cause the optimization scheme obtained by the NSGA-Ⅱ to be inaccurate. To verify the feasibility and accuracy of the optimization results, a simple experiment was conducted. The test material and conditions were the same as those used in Section 2.1, and considering the feasibility of validation test in reality, the operating parameters of the separation device were adjusted to x_1 = 39°, x_2 = 36°, x_3 = 21 m/s, and x_4 = 13.5 m/s, respectively. A comparison of prediction results and experimental results is shown in Table 4. The final measured values (average of three experiments) of the impurity rate and loss rate were 4.51% and 6.62%, respectively, which are close to the predicted values within the acceptable limits of the error percentage (3.20% and 3.60%). The combination of RSM, ANN, and NSGA-Ⅱ can help guide the designer in choosing walnut shell-kernel separation device parameters based on the optimization results to achieve an effective, high-quality, and economical separation.

Table 4 Comparison of optimized prediction results and experimental results

No.	x_1/(°)	x_2/(°)	x_3/m·s^{-1}	x_4/m·s^{-1}	y_1/%	y_2/%
Predict	38.78	36.10	20.93	13.50	4.37	6.39
Experiment	39	36	21	13.5	4.51	6.62
Error/%	0.57	0.27	0.33	0	3.20	3.60

The final optimization results showed an optimal wind speed of 21 m/s (equivalent to a force of eight gales, China Meteorological Administration), which is sufficient to destroy tree branches. The wind speed of the separation is related to the particle size, frontal area, and density of the walnut shell and kernel. Due to the small particle size and frontal area of walnut shells and kernels, a larger wind speed is required under the same airflow conditions. This phenomenon is consistent with the results in Li et al.[9], Chen et al.[40], and Chai et al.[41], where similar wind speed (16-30 m/s) requirements were observed for shell kernel separation experiments. Furthermore, another possible cause of excessive wind speed may be related to the structural effect of the separation equipment on the airflow's kinetic properties. This design may allow the airflow to accelerate as it passes through the separation chamber, resulting in higher wind speeds. This phenomenon is consistent with Lu et al.[42], which verifies the effect of the structure of the 90° elbow on the flow field distribution through numerical simulations and experiments. Therefore, the wind speed requirement in this study is mechanistically consistent with the findings of the above literature, providing a theoretical basis and practical guidance for optimizing the separation process.

4 Discussion

In terms of the walnut shell-kernel separation, various methods have been explored, but each one with limitations. Intelligent visual identification is highly accurate but faces challenges due to the similarity between shells and kernels and the need for specialized knowledge. Pneumatic separation, however, offers higher efficiency, lower costs, and easier operation. Among pneumatic separators, two-stage systems have shown superior accuracy and efficiency compared to single-stage or multi-stage systems. The two-stage tandem walnut shell-kernel separation device designed in this study significantly enhanced separation efficiency and accuracy by using deflector plates and a tandem configuration. The deflector plates prevented centrifugal motion along the inner wall of the bend pipe, dispersing material movement and improving separation performance. The tandem configuration added an additional separation stage, simplifying the process and achieving purer separation.

Compared with the single-stage technologies of Niu et al.[46] (the device previously developed by our team) and Li et al.[9] (the device previously developed by our team), the present design achieved a significant reduction in impurity rate by 73.98% and 77.55%, respectively, under identical conditions, with a corresponding decrease in loss rate of 9.44% and 53.96%. Compared with multi-stage separation devices, our design demonstrated comparable impurity rates and loss rates to the walnut shell and kernel separator[19] (IR = 4.75% and LR = 8.41%) and the airflow separation system[47] (IR = 5.57% and LR = 6.85%), but with a substantial enhancement in processing capacity of more than 200%. Also, our design processed 720 kg/h, which is 33.33% higher than the 540 kg/h of the walnut shell and kernel separator[19] and negative pressure winnowing device[40]. In summary, the optimized two-stage tandem separation device that features specially designed deflector plates and a tandem configuration, offers significant advantages in walnut shell-kernel separation by enhancing separation performance and improving the separation of high-quality kernels, broken kernels, and shells.

Previous studies on multi-duct separators focused on optimizing individual units, but two-stage separators are complex systems influenced by multiple factors with nonlinear relationships. RSM can address linear relationships but is limited in handling nonlinear ones, while ANN can capture complex relationships but requires large datasets to avoid overfitting. This study combines RSM and ANN to reduce data and computation costs, using RSM data for ANN training. Additionally, NSGA-Ⅱ is employed for global optimization, overcoming RSM's local optima limitations. This combined approach enhances prediction accuracy and

separation performance. However, incomplete separation remains an issue, highlighting the need for further improvements in the two-stage tandem separator design.

(1) Walnut kernel damage and separation efficiency

In this study, the primary objective is to enhance the separation device's performance by maximizing efficiency while minimizing impurity and loss rates. Potential kernel damage or energy penalties associated with high air velocities (e.g., 21 m/s) are not addressed herein. Future work should quantify how physical properties (variety, moisture, shell-kernel gap, particle size), operating parameters (air velocity, gap, angle), and equipment design (contact-surface material) collectively influence kernel damage to establish a universal prediction model.

(2) Energy consumption and separation efficiency

Although the current optimization model does not explicitly include energy consumption constraints, enhanced separation efficiency achieved through optimized parameters shortens residence time and thereby reduces energy demand. Nevertheless, actual energy consumption is modulated by regional electricity tariffs, cumulative operating hours, and throughput, all of which must be assessed in specific operating environments. Future studies should therefore incorporate energy consumption as an explicit constraint within the optimization framework to deliver an integrated solution that simultaneously maximizes separation efficiency and minimizes energy consumption.

(3) Particle-fluid interactions

This study optimizes separation equipment parameters using RSM, ANN, and NSGA-Ⅱ to improve efficiency by reducing impurity and loss rates. CFD and a continuous phase model are used to efficiently optimize structural parameters like bend radii, saving experimental costs and time. Future work is needed to explore particle trajectories and interactions to address the complex particle-fluid dynamics and further enhance separation efficiency.

Table 5 Comparison of different types of walnut shell kernel air separation separators

Typology	Equipment name	Units	Capacity	Separation performance
Intelligent visual identification technique	Fuzzy clustering algorithm[43]	1	100 walnuts	RR = 83%
	YOLOX deep learning algorithm[44]	1	2753 photos	RR = 96.3%
	Near-infrared spectroscopy[4]	1	1200 units	RR = 97.78%
	An enhanced YOLOv8n algorithm[45]	1	not stated	RR = 93.56%
Pneumatic separation method	Separation device of walnut shell and kernel[46]	1	5 kg (constant)	IR = 17.33%, LR = 7.31%
	Walnut shell-kernel winnowing device[9]	1	3 kg (constant)	IR = 20.09%, LR = 14.38%
	Positive pressure pneumatic separation device[10]	1	3 kg (constant)	IR = 8.14%, LR = 4.42%
	Airflow separation system[47]	4	21-360 kg/h	IR = 5.57%, LR = 6.85%
	Negative pressure winnowing device[40]	3	540 kg/h	IR 4%-8%, LR 0.41-1.22%
	Winnowing machine[48]	4	150-240 kg/h	IR 3.5%-6.54%, LR 0.68%-1.19%
	Walnut shell and kernel separator[19]	2	540 kg/h	IR = 4.75%, LR = 8.41%
	This design	2	720 kg/h	IR = 4.51%, LR = 6.62%

Note: "RR" is recognition rate, "IR" is impurity rate, and "LR" is loss rate.

5 Conclusions

To solve the walnut shell-kernel separation problem, the present work describes an engineering solution, i.e., the design and optimization of a two-stage tandem walnut shell-kernel separation device. The analysis results of spatial flow field distribution in a separation duct show that when the radius of the duct is 550 mm, the pressure and the velocity flow field are more uniform. The RSM and ANN have been used to optimize operating parameters for a walnut shell-kernel separation device and compare their predictive performance. The results show that the combination of RSM and ANN is an effective means to enhance the optimization performance. This integrated approach significantly reduces the number of simulations and improves the modeling predictive accuracy. The data collected by RSM provides a solid foundation for constructing highly accurate ANN models. Also, the ANN model is more accurate and reliable (higher R^2, lower MSE and RMSE), which is because it fits the experimental data's nonlinear features better. Finally, the ANN model was optimized using NSGA-Ⅱ, and the optimal values of the objective function impurity rate and loss rate are 4.51% and 6.62%, respectively. Compared with traditional single-stage devices, the optimized device reduced impurity rate by 73.98% to 77.55% and loss rate by 9.44% to 53.96%, significantly improving separation efficiency and quality. The combination of RSM, ANN, and NSGA-Ⅱ was confirmed to be a beneficial tool for optimizing machine performance.

Acknowledgements

This work has been financially supported and encouraged by the National Science Foundation for Young Scientists of China (Grant No. 12002229), the Key R&D Program Projects of Xinjiang Uygur Autonomous Region (2024B02017), the Bingtuan Science and Technology Program (Grant No. 2022CB008, 2018CB014), the Science and Technology Research Project of the Presidential Foundation of Tarim University (Grant No. TDZKBS202414), and the National Forestry and Grassland Equipment Science and Technology Innovation Park's "Challenge System" Major Breakthrough Project (2024YG06).

[References]

[1] Man X L, Li L, Zeng Y, Tang Y R, Yang J L, Fan X W, et al. Mechanical impact characteristics of hollow shell granule based on continuous damage theory. Powder Technology, 2023; 429: 118946.

[2] Chen C, Pan Z L. Postharvest processing of tree nuts: Current status and future prospects—A comprehensive review. Comprehensive Reviews in Food Science and Food Safety, 2022; 21(2): 1702–1731.

[3] Zhang X, Meng J, Shi X M, Fang X P. Application status of walnut shell separation technology. China Oils Fats, 2021; 46(6): 137–140. (in Chinese)

[4] Liu M Z, Li C H, Cao C M, Wang L Q, Li X P, Che J, et al. Walnut fruit processing equipment: academic insights and perspectives. Food Engineering Reviews, 2021; 13(4): 822–857.

[5] An M H, Cao C M, Wu Z M, Luo K. Detection method for walnut shell-kernel separation accuracy based on near-infrared spectroscopy. Sensors, 2022; 22(21): 8301.

[6] Rong D, Xie L J, Ying Y B. Computer vision detection of foreign objects in walnuts using deep learning. Computers and Electronics in Agriculture, 2019; 162: 1001–1010.

[7] Wang Z C, Xiao W Z. Electrostatic kernel separator. 1989; CN2041490, 7-26. (in Chinese)

[8] Krishnan P, Berlage A G. Separation of shells from walnut meats using magnetic methods. Transactions of the ASAE, 1984; 27(6): 1990–1992.

[9] Li H, Tang Y R, Zhang H, Liu Y, Zhang Y C, Niu H. Technological parameter optimization for walnut shell-kernel winnowing device based on neural network. Frontiers in Bioengineering and Biotechnology, 2023; 11: 1107836.

[10] Zhang Q. Optimization and experimental study of positive pressure pneumatic walnut shell and kernel separation device. Xinjiang, China: Tarim University, 2023. (in Chinese) DOI: 10.27708/d.cnki.gtlmd.2023.

000231.

[11] Safikhani H. Modeling and multi-objective Pareto optimization of new cyclone separators using CFD, ANNs and NSGA Ⅱ algorithm. Advanced Powder Technology, 2016; 27(5): 2277–2284.

[12] Lim B Y, Shamsudin R, Baharudin B H T, Yunus R. Performance evaluation and CFD multiphase modeling for Multistage Jatropha Fruit Shelling Machine. Industrial Crops and Products, 2016; 85: 125–138.

[13] Chen P Y, Han Y L, Jia F G, Zhao D, Meng X Y, Li A Q, et al. Investigation of the mechanism of aerodynamic separation of rice husks from brown rice following paddy hulling by coupled CFD-DEM. Biosystems Engineering, 2022; 218: 200–215.

[14] Li D, Zhong H D, Yin W Z, Hu Y. Classification-dispersion flotation of fine mixed magnetic concentrate. Journal of Northeastern University (Natural Science), 2021; 42(12): 1761–1767. (in Chinese)

[15] Wang S, Yang Y, Yang X L, Zhang Y D, Zhao Y M. Dry beneficiation of fine coal deploying multistage separation processes in a vibrated gas-fluidized bed. Separation Science and Technology, 2019; 54(4): 655–664.

[16] Park C W, Song D H, Yook S J. Development of a single cyclone separator with three stages for size-selective sampling of particles. Journal of Aerosol Science, 2015; 89: 18–25.

[17] Duan X Q, Zhou P Y. A design and improvement scheme of rubber roller husker. Grain Processing, 2019; 204(6): 73–74. (in Chinese)

[18] Shi Q X, Ma M, Yan W H, Zhou H, Yuan H J, Li Y H. Two-stage winnower cyclone separating cleaning system performance testing and optimization. Transactions of the CSAM, 2014; 45(11): 124–128. (in Chinese)

[19] Zhang L, Liu H. Optimization and experiment of operating parameters for walnut shell and kernel separator. Anhui Agricultural Science Bulletin, 2025; 31(2): 108–115. (in Chinese)

[20] Zhang H, Liu H L, Zeng Y, Tang Y R, Zhang Z G, Che J. Design and performance evaluation of a multi-point extrusion walnut cracking device. Agriculture, 2022; 12(9): 1494.

[21] Liu T Y, Xu X Y, Li C B, Jiao H J. Numerical simulation of internal flow field in 90° rectangular bend pipe under different curvatures. Machinery, 2021; 48(1): 6–13. (in Chinese)

[22] Dai F, Song X F, Guo W J, Zhao W Y, Zhang F W, Zhang S L. Simulation and test on separating cleaning process of flax threshing material based on gas-solid coupling theory. Int J Agric & Biol Eng, 2020; 13(1): 73–81.

[23] Le D K, Yoon J Y. Numerical investigation on the performance and flow pattern of two novel innovative designs of four-inlet cyclone separator. Chemical Engineering and Processing-Process Intensification, 2020; 150: 107867.

[24] Sun J F, Chen H M, Duan J L, Liu Z, Zhu Q C. Mechanical properties of the grooved-wheel drilling particles under multivariate interaction influenced based on 3D printing and EDEM simulation. Computers and Electronics in Agriculture, 2020; 172: 105329.

[25] Srikanth V, Rajesh G K, Kothakota A, Pandiselvam R, Sagarika N, Manikantan M R, et al. Modeling and optimization of developed cocoa beans extractor parameters using box behnken design and artificial neural network. Computers and Electronics in Agriculture, 2020; 177: 105715.

[26] Gupta S, Patel P, Mondal P. Biofuels production from pine needles via pyrolysis: Process parameters modeling and optimization through combined RSM and ANN based approach. Fuel, 2022; 310: 122230.

[27] Salari M, Nikoo M R, Al-Mamun A, Rakhshandehroo G R, Mooselu M G. Optimizing Fenton-like process, homogeneous at neutral pH for ciprofloxacin degradation: Comparing RSM-CCD and ANN-GA. Journal of Environmental Management, 2022; 317: 115469.

[28] Huang T, Rong L, Zhang G Q. Investigating the feasibility of using computational fluid dynamics based response surface methodology and neural network to model the performance of the individualised ventilation in sow houses. Biosystems Engineering, 2022; 214: 138–151.

[29] Liu H, Tana, Zhen Q, Hurichabilige, Meng X, Li W. Environ-economic assessment of the solar coupled heat pump heating system for dairy barns in severe cold region. Energy and Buildings, 2025; 328: 115166.

[30] Zhang N, Fu J, Chen Z, Chen X G, Ren L Q. Optimization of the process parameters of an air-screen cleaning system for frozen corn based on the response surface method. Agriculture, 2021; 11(8): 794.

[31] Wang L J, Yu Y T, Ma Y, Feng X, Liu T H. Investigation of the performance of different cleaning devices in maize grain harvesters based on field tests. Transactions of the ASABE, 2020; 63(4): 809–821.

[32] Yang M Y, Zhang K Y, Shu M Y, Deng K Y. Experimental study on unsteady flow field in a centrifugal compressor at pulsating backpressure conditions. Aerospace Science and Technology, 2020; 106: 106168.

[33] Zhang Z, Shao M S, Ling X. Experimental study on the separation performance of a novel gas–liquid separator. Advanced Powder Technology, 2022; 33(11): 103795.

[34] Duan, J H, Gao S, Hou C G, Wang W W, Zhang P, Li C J. Effect of cylinder vortex stabilizer on separator performance of the Stairmand cyclone. Powder technology, 2020; 372: 305–316.

[35] Ma H C, Dai C, Dong L, Wu X F. PIV experiment of inner flow field in 90° bending ducts with square section. Advances in Science and Technology of Water Resources, 2013; 33(5): 31–34, 56. (in Chinese)

[36] Zhang C, Li A G, Li J X, Hou Y C, Chen Xing. Radiation noise control of a 90 rectangular elbow in ventilation and air conditioning systems. Journal of Building Engineering, 2021; 37: 102157.

[37] Jiang G D, Sun L P, Shi L B, Jin K A, Huang G R, Wu Z R. Numerical study on the flow and heat transfer characteristics in a 90°-bend extruded pipe set in water-cooled plate. Fluid Machinery, 2023; 51(4): 51–57, 90. (in Chinese)

[38] Du X Q, Xiao M H, Hu X Q, Chen J N, Zhao Y. Numerical simulation and experiment of gas-solid two-phase flow in cross-flow grain cleaning device. Transactions of the CSAE, 2014; 30(3): 27–34. (in Chinese)

[39] Nayak P K, Chandrasekar C M, Gogoi S, Krishnan Kesavan R. Impact of thermal and thermosonication treatments of amora (Spondius pinnata) juice and prediction of quality changes using artificial neural networks. Biosystems Engineering, 2022; 223: 169–181.

[40] Chen X D, Hu G Y, Zhao T F, Li Z X, Zhou J P. Simulation study on negative pressure winnowing of walnut kernel mixture based on CFD-DEM coupling. Journal of Shandong Agricultural University (Natural Science Edition), 2021; 52(6): 1017–1027. (in Chinese)

[41] Chai X Y, Xu L Z, Sun Y X, Liang Z W, Lu E, Li Y M. Development of a cleaning fan for a rice combine harvester using computational fluid dynamics and response surface methodology to optimise outlet airflow distribution. Biosystems Engineering, 2020; 192: 232–244.

[42] Lu Y G, Hu Z C, Lin D Z, Yu Z Y, You Z Y, Wu Nu. Numerical simulation of peanuts particles conveying in pipeline using CFD-DEM coupled approach. Journal of Chinese Agricultural Mechanization, 2016; 37(6): 104–109. (in Chinese)

[43] Wang T Y, Cao C M, Xie C J, Li Z. Design of hickory nuts' shell and kernel sorting system based on fuzzy clustering algorithm. Food & Machinery, 2018; 34(6): 110–114, 157. (in Chinese)

[44] Zhang Y, Wang X, Liu Y, Li Z, Lan H, Zhang Z, et al. Machine vision-based Chinese walnut shell–kernel recognition and separation. Applied Science, 2023; 13: 10685.

[45] Ni P, Hu S, Zhang Y, Zhang W, Xu X, Liu Y, et al. Design and optimization of key parameters for a machine vision-based walnut shell–kernel separation device. Agriculture, 2024; 14: 1632.

[46] Niu H. Experimental study and design of separation device of walnut shell and kernel. Xinjiang, China: Tarim University, 2020. (in Chinese) DOI: 10.27708/d.cnki.gtlmd.2020.000106.

[47] Zhu Z J, Kang M, Liu K, Yang L L, Yang Z Q, Zhu Z S. Experimental study on airflow separation system of walnut shell and kernel mixed materials. China Oils and Fats, 2022; 47(3): 137–142. (in Chinese)

[48] Hu G Y, Chen X D, Dong Y L, Liu G, Zhou J P. Optimization and experiments on working parameters of winnowing machine for walnut shell and kernel mixture. Food & Machinery, 2023; 39(5): 83–88. (in Chinese)